Processing maps and microstructural evolution of the type 347H austenitic heat-resistant stainless steel

Yinghui Zhou, Yongchang Liu,[a] Xiaosheng Zhou, Chenxi Liu, Liming Yu, and Chong Li
State Key Lab of Hydraulic Engineering Simulation and Safety, School of Materials Science & Engineering, Tianjin University, Tianjin 300072, People's Republic of China

Baoqun Ning
School of Materials Science and Engineering, Tianjin University of Technology, Tianjin 300384, People's Republic of China

(Received 7 March 2015; accepted 26 May 2015)

To study the thermal deformation behavior and microstructural evolution of the type 347H austenitic steel, compression experiments were conducted at the temperatures of 800–1100 °C with strain rates of 0.01–10 s^{-1}. The activation energy and constitutive equation of the type 347H steel during thermal deformation process were determined according to the flow stress curves. Both the hot processing maps and microstructure characteristics under different deformation conditions were investigated. Based on the thermal processing maps, two unstable regions under 800 °C/0.01–10 s^{-1} and 1100 °C/0.01 s^{-1} were identified. The processing maps were in favor of optimizing thermal processing parameters and improving thermal processing properties of the type 347H austenitic steel. After thermal deformation, the dislocation in the austenite matrix increases significantly. Besides, in the stable regions, the precipitation of carbides is facilitated by thermal deformation.

I. INTRODUCTION

Nowadays, countries worldwide have been developing supercritical and ultrasupercritical generators to reduce pollution and lower costs. Power generation efficiency is affected by generator efficiency, combustion chamber efficiency, coupling efficiency, and so on. To improve the Carnot cycle efficiency, lots of countries have been developing heat-resistant steels. 18Cr–8Ni type austenitic steels have been the focus of many studies due to their excellent combination of high ductility, strength, and steam oxidation resistance at high temperatures. And they are widely used in boiler, petroleum, and other industries.[1–3] As one of 18Cr–18Ni type austenite steels, the niobium (Nb)-bearing austenitic stainless steel is frequently used in coal-fired power plants.

Over the past decades, a great deal of research activities about austenitic heat-resistant steels has been focused on creep behavior and microstructural evolution at high temperatures,[4–7] whereas little attention has been paid to the thermal deformation performance and the carbides precipitation of the austenitic stainless steel. Actually, the hot deformation processing maps of heat-resistant steels are favorable to optimize the workability and control the microstructures of the materials.[8] Liu et al. defined the processing map of Ni-base superalloy.[9] Nkhoma et al. revealed the hot working characteristics of 321 steel and 304 steel.[10] In addition, Farahat et al. pointed out that the mechanical properties could be improved with the increase in both the cold deformation strain and the Nb content.[11] Using constitutive equations and processing maps, Momeni and Deghani explored the characterization of thermal deformation behaviors of 410 martensitic stainless steel and 2205 austenite–ferrite duplex stainless steel.[12,13]

In this study, the constitutive equation and the processing maps of type 347H austenitic steel were established to understand the thermal deformation mechanisms. Furthermore, the influences of working temperature and strain rate on microstructural evolution of type 347H austenitic steel were also explored.

II. EXPERIMENTAL DETAILS

The chemical composition of the investigated type 347H austenitic steel is given in Table I. The cylindrical specimens with a size of Ø 8 mm × 12 mm were machined for hot working. Using a Gleeble-3500 thermal mechanical simulator (Dynamic Systems Inc., Poestenkill, NY), specimens were heated to 1150 °C for 5 min and then cooled to 800, 900, 1000, and 1100 °C, respectively. The hot compression of the samples was performed with the strain rates from 0.01 to 10 s^{-1}. All of the samples were compressed to a true strain of 0.6. The specimens were etched with a mixed solution

Contributing Editor: Jürgen Eckert
[a]Address all correspondence to this author.
e-mail: licmtju@163.com
DOI: 10.1557/jmr.2015.168

TABLE I. Chemical composition of the explored type 347H austenitic steel (in weight percent).

Element	C	Cr	Ni	Nb	Si	Mn	P	Mo	S	Fe
wt%	0.06	17.60	10.71	0.54	0.34	1.59	0.02	0.12	0.01	Balance

($CuCl_2$:HCl:CH_3CH_2OH = 1:20:20, in volume). Microstructures and phase identifications were examined using a scanning electron microscope (SEM) equipped with an energy dispersal spectrometer and a transmission electron microscope (TEM) operated with a voltage of 200 kV. The TEM samples were first mechanically ground to a 50 μm thick plate and then thinned using the DJ-2000 type electrolytic device.

III. RESULTS AND DISCUSSION

A. Constitutive equation of type 347H austenitic steel

It is well-known that the effects of strain rate and temperature under hot deformation condition are incorporated in the Zener–Hollomon parameter.[14–17] Besides, the relationship of the Zener–Hollomon parameter and flow stress is commonly established via the constitutive equation, as follows[10,18]:

$$Z = \varepsilon \exp\left(\frac{Q}{RT}\right) = A\left[\sinh\left(\alpha\sigma_p\right)\right]^n \quad , \qquad (1)$$

where σ is the flow stress, ε is the strain rate, Q is the deformation activation energy, R is the gas constant, T is the deformation temperature, and A, α, and n are the material constants, respectively. According to Eq. (1), the following relation is given as:

$$\ln \varepsilon = \left(\ln A - \frac{Q}{RT}\right) + n \ln \sinh\left(\alpha\sigma_p\right) \quad . \qquad (2)$$

Based on the Eq. (2), determination of the constants is the key to compute the constitutive equation. Figure 1(a) reveals the variation of stress corresponding to the peak with strain rate at different deformation temperatures. By applying linear regression of the data, the average values of α and n are obtained as 8.7 and 0.0062, respectively. To determine the empirical values of Q and A, the Eq. (2) can be written as below:

$$\ln \sinh\left(\alpha\sigma_p\right) = \left(\frac{\ln \varepsilon - \ln A}{n}\right) + \frac{Q}{nRT} \quad . \qquad (3)$$

Figure 1(b) indicates the variation of flow stress with reciprocal temperature. The Eq. (3) shows that the average slope of linear regressed data is Q/RT, while the average intercept is A.[19] According to the data, the values of A and Q are 2.8×10^{21} and 555.1 kJ, respectively. Therefore, the constitutive equation of the explored type 347H austenitic heat-resistant steel can be obtained as follows:

$$Z = \varepsilon \exp\left(\frac{555100}{RT}\right) = 2.8 \times 10^{21}\left[\sinh\left(0.0062\sigma_p\right)\right]^{8.7} \quad . \qquad (4)$$

B. Processing maps of type 347H austenitic steel

Dynamic material model (DMM) is widely used to explain the hot workability of metal materials. Based on DMM, the processing maps were recently proposed by Prasad and Sivakesavam.[20] Thus, the energy dissipation equation is given as follows:

$$P = \sigma\varepsilon = \int_0^{\varepsilon} \sigma d\varepsilon + \int_0^{\sigma} \varepsilon d\sigma = G + J \quad , \qquad (5)$$

where σ is the stress and ε is the strain rate. The overall power P consists of two complementary parts, the power dissipation capacity, G, which is related to plastic deformation of the material dissipation and the power dissipation value, J, which is relevant to microstructural evolution during deformation, such as dynamic recovery and recrystallization, and phase transformation induced by deformation. The constitutive equation is:

$$\sigma = K\varepsilon^m \quad , \qquad (6)$$

where K is a constant, m is the sensitivity index of strain rate varying from 0 to 1. The sensitivity index is an important indicator of the expression of metal superplasticity, and m can be defined as follows:

$$\frac{dJ}{dG} = \frac{\varepsilon d\sigma}{\sigma d\varepsilon} = \frac{d\sigma}{\sigma}\left(\frac{d\varepsilon}{\varepsilon}\right)^{-1} = \frac{d\ln\sigma}{d\ln\varepsilon} = m \quad . \qquad (7)$$

The flow stress values under various deformation temperatures and strain rates are listed in Table II. By using cubic spline interpolation, the dependency of m on deformation temperatures and strain rates is determined as shown in Fig. 2(a). For the explored type 347H austenitic steel, the obtained m values vary from 0.02 to 0.2. Increase of temperature and decrease of strain rate result in increase of the values of m. Under the low strain rate and high deformation temperature, the type 347H steel exhibits a better characteristic of plastic deformation.[21,22]

According to Eqs. (5)–(7), the relationship between the power dissipation association J and the sensitivity index of strain rate m could be described by the following equation[12]:

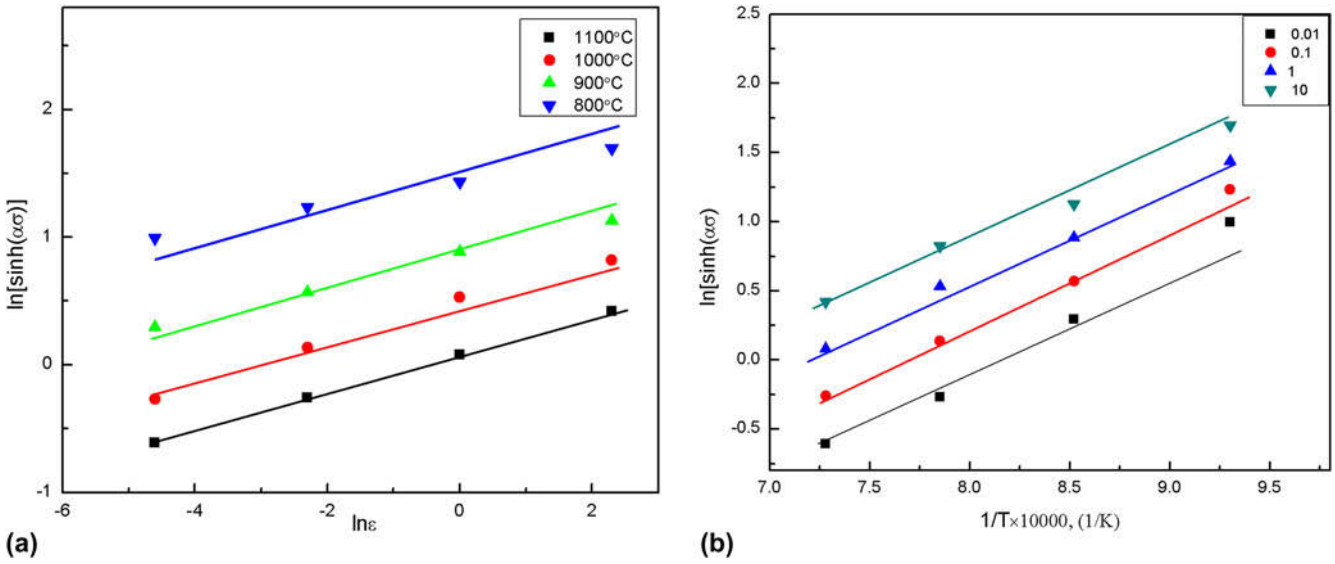

FIG. 1. (a) Variation of hyperbolic sine function of peak stress with strain rate at various deformation temperatures for determination of related constants of n and α. (b) Variation of hyperbolic sine function of peak stress with strain rate at various strain rates for determination of apparent activation energy, Q, and constant, A.

TABLE II. Flow stress values of the explored type 347H austenitic steel.

	Temperature (°C)			
Strain rate (s^{-1})	1100	1000	900	800
0.01	71.5	93.2	169.9	273.5
0.1	94.9	116.4	208.4	301.4
1	141.8	204.1	271.1	338.8
10	186.6	242.7	293.6	347.4

$$J = \int_0^{\sigma} \varepsilon d\sigma = \frac{\sigma\varepsilon m}{m+1} \quad , \tag{8}$$

When m reaches to 1, J reaches the maximum. The power dissipation efficiency η, indicating the proportion of power dissipation arising from microstructural evolution (dynamic recovery and recrystallization), would be defined as:

$$\eta = \frac{J}{J_{\max}} = \frac{2m}{m+1} \times 100\% \quad . \tag{9}$$

Based on DMM, η is a dimensionless parameter that can be used to assess the workability of the materials under certain deformation temperature and strain rate. In general, the larger η is, the better the workability will be. As shown in Fig. 2(b), the contour plots of the power dissipation efficiency η and m of the type 347H steel seem exactly the same. The η varies from 2 to 32%. Increase of the deformation temperature and the decrease of strain rate lead to the increase of the η. Large η value suggests that the microstructure evolution takes a large amount of power dissipation, meaning that dynamic recovery and recrystallization are more prone to occur. The plot of η variation as a function of deformation temperature and strain rate is defined as the power dissipation map. For metals, dynamic recrystallization is generally considered as the best thermal deformation mechanism, since the defects in materials can be removed, and the microstructure will be restored. Under large strain rates, the deformed microstructure does not have enough time to recovery and recrystallize, and cracks and voids are produced in the matrix. To avoid these defects, the stable and unstable zones of thermal deformation should be clarified. By introducing the instability parameter, ξ, the relation of stress and strain rate can be expressed as:

$$\xi(\varepsilon) = \frac{\partial \ln[m/(m+1)]}{\partial \ln \varepsilon} + m \quad . \tag{10}$$

The thermal deformation areas with $\xi < 0$ are considered as an unstable region. Substitute the data shown in the values of m into Eq. (10), instability parameter contour map of the type 347H steel is obtained. To determine instability region, the instability parameter value is set to zero. Figure 2(b) represents the instability map of type 347H steel. It can be seen that the gray unstable regions mainly locate in the area where strain rate is relatively fast, and the deformation temperatures is relatively low.

Combining the energy dissipation efficiency map and unstable zone map, the material thermal processing map can be obtained. Thermal processing maps can visually

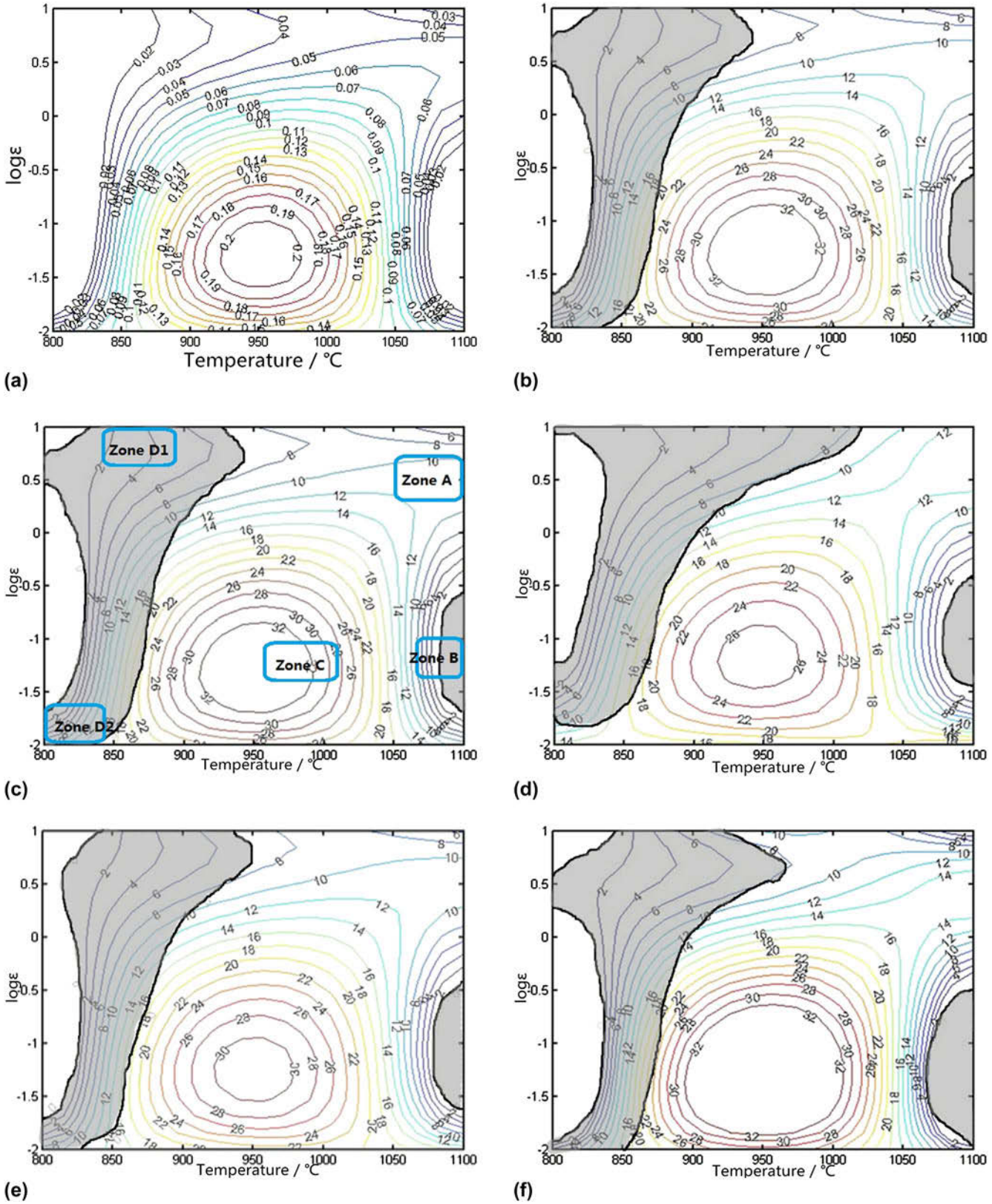

FIG. 2. The processing maps of the explored type 347H austenitic steel. (a) The determined *m* values, (b) the processing map with a true strain of 0.6, (c) the processing map indicating different deformation regions A, B, C, and D, (d) the processing map with a true strain of 0.2, (e) the processing map with a true strain of 0.4, and (f) the processing map with a true strain of 0.8.

show the unstable zone and safe zone of materials. Safe zone generally includes dynamic recrystallization regions, superplasticity areas, and dynamic recovery areas. Some processing zones that are unstable should be avoided, such as empty zones, wedge zones, grain boundary cracking zones, and adiabatic shear band formation areas.[23,24] Based on processing maps, the thermal processing parameters can be optimized. Figure 2(b) is the processing map of type 347H austenitic steel (the applied strain is 0.6), and the regions colored in gray are unstable zones. It is found that η values in the unstable areas are slightly smaller than those in other areas. The processing maps of the type 347H austenitic steel under different strains (0.2, 0.4, and 0.8) are shown in the Figs. 2(d)–2(f), respectively. The area of unstable region is the smallest when the strain is 0.4. It is worth noting that the areas of unstable zones are large when the thermal deformation strain is too large or too small. In other words, the available optimal machining parameters for the hot deformation are limited.

C. Effects of thermal deformation on microstructure of type 347H austenitic heat-resistant steel

Based on the processing map of type 347H austenitic steel, five typical regions [see Fig. 2(c)] are selected to analyze the microstructure evolution during thermal deformation. For a direct comparison, the microstructure of the undeformed specimen is also represented in Fig. 3(f). Some twins can be found inside of the austenite grains.[25,26]

(i) The SEM micrograph corresponding to zone A (deformation temperature is 1100 °C and the strain rate is 1 s^{-1}), where m value is about 0.06 and η value (the energy dissipation efficiency) is 10%, is shown in Fig. 3(a). In this area, full dynamic recrystallization takes place. Equiaxial recrystallized austenite grains are formed with a much less grain size than that of the sample without thermal deformation. In addition, the grains are more homogeneously distributed, which indicate that zone A is a safe zone for hot working.

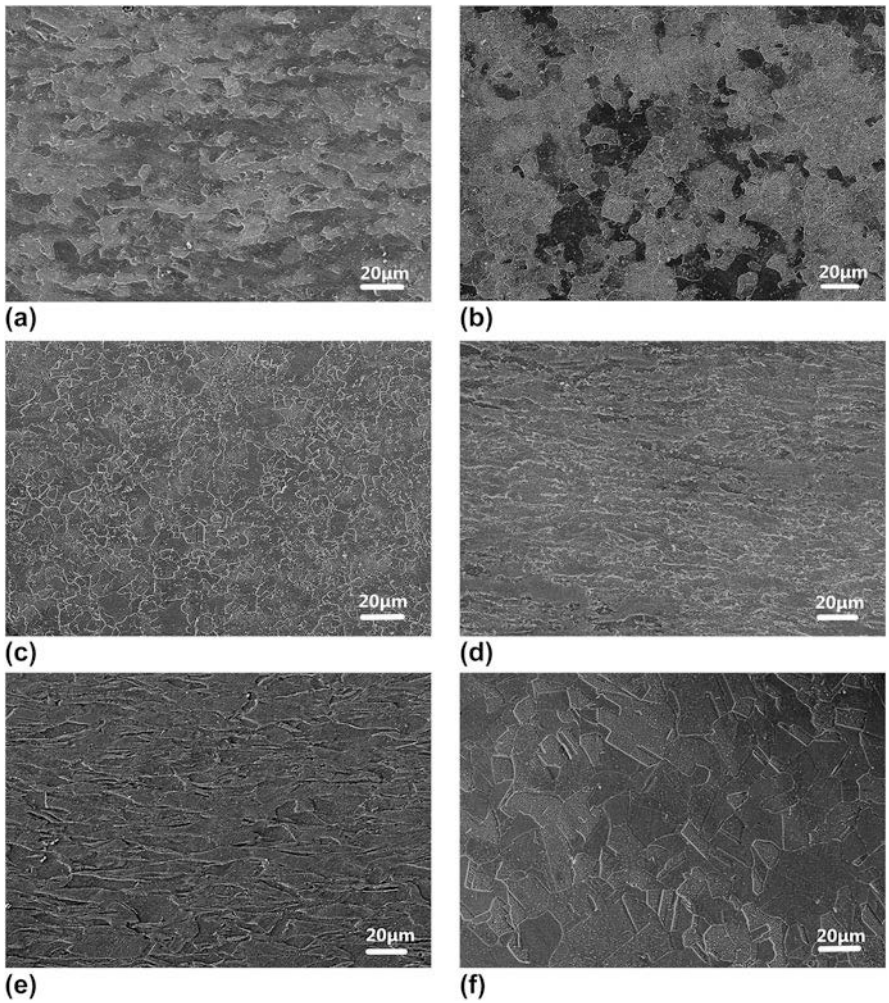

FIG. 3. Typical microstructures of type 347H austenitic steel after hot compression under the conditions of (a) 1100 °C; 1 s^{-1}, (b) 1100 °C; 0.1 s^{-1}, (c) 1000 °C; 0.1 s^{-1}, (d) 800 °C; 10 s^{-1}, (e) 800 °C; 0.01 s^{-1}, and (f) undeformed.

(ii) The SEM micrograph corresponding to zone B (deformation temperature is 1100 °C and the strain rate is 0.1 s^{-1}), where m is about 0.02 and η is 2%, is shown in Fig. 3(b). It is noted that the unstable parameter is less than 0, suggesting that Zone B is an unstable region. The calculated η value represents the workability of materials. The higher the η value is, the better plasticity of the steel will exhibit. That is to say, dynamic recrystallization is not easy to occur when the steel is deformed at zone B. Though discontinuously recrystallized grains can be observed in the matrix, the grains are connected with each other. It is well-known that grain boundary sliding mechanism is a typical deformation mechanism of metallic materials in this thermoplastic area.[27] The recrystallized grains connect to each other, and the grain boundary area is too small to hinder the movement of dislocation. Furthermore, a few coarse carbide particles precipitate along the grain boundaries, which can cause

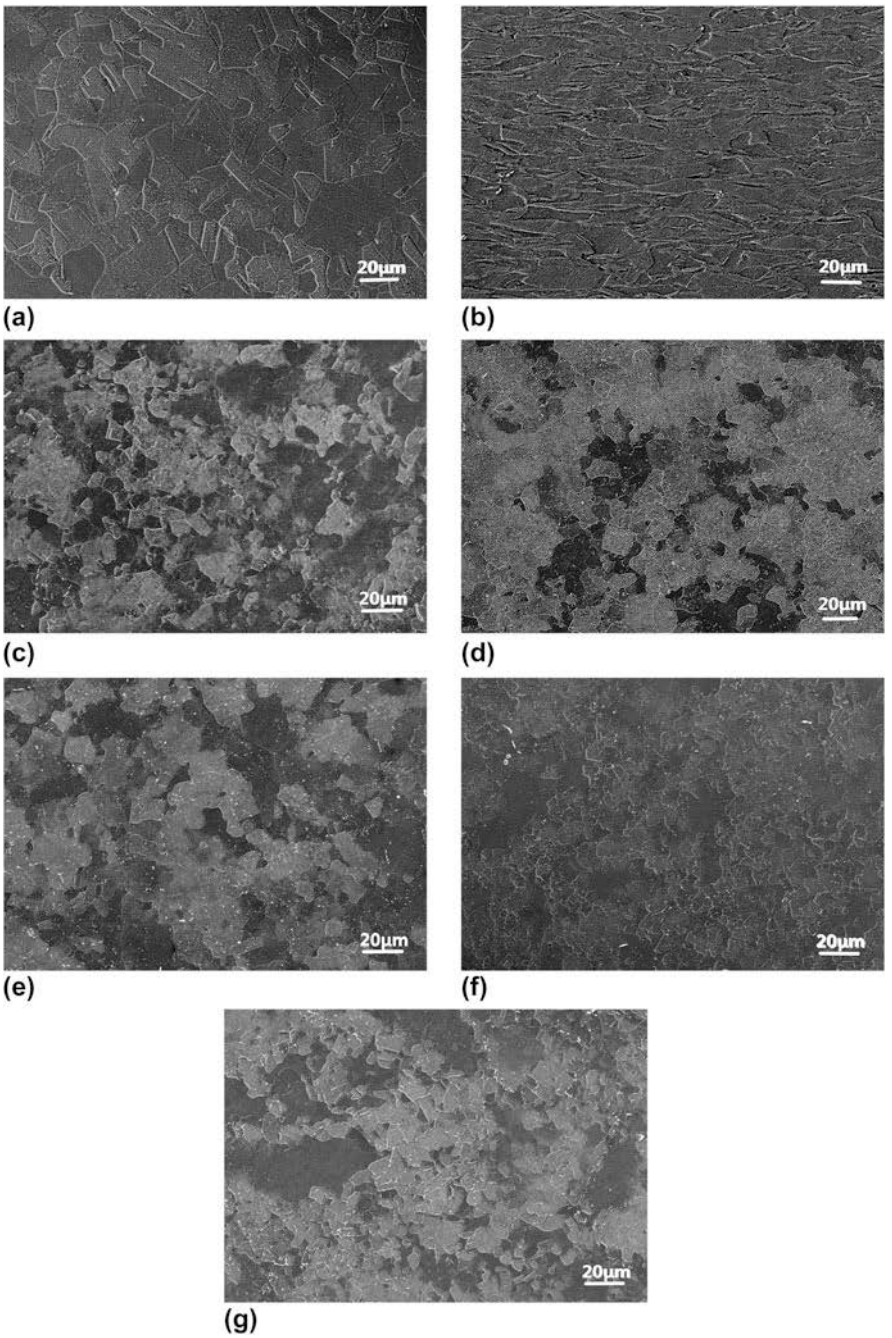

FIG. 4. Microstructures of the quenched specimens after austenization at 1150 °C for 30 min and compressively deformed at different conditions, (a) undeformed, (b) 800 °C; 0.01 s^{-1}, (c) 1000 °C; 0.01 s^{-1}, (d) 1100 °C; 0.01 s^{-1}, (e) 1100 °C; 0.1 s^{-1}, (f) 1100 °C; 1 s^{-1}, and (g) 1100 °C; 10 s^{-1}.

the deformation instability. Thus, Zone B can be classified as a typical unstable region, and the deformation parameters should be avoided.

(iii) The SEM micrograph corresponding to Zone C (deformation temperature is 1000 °C and the strain rate is 0.1 s^{-1}), where m value is about 0.19 and η is 30%, is shown in Fig. 3(c). Due to the high-energy dissipation efficiency, dynamic recrystallization will occur, which is consistent with the law of the stress–strain curve. As the deformation temperature reaches to 1000 °C, recrystallized grains on prior austenite boundaries will be produced significantly, and the sizes of them gradually increase. Although the strain rate is decreased, deformation temperature is lower than that of zone A. Thus, the recrystallized grains cannot grow up fast and the size is smaller than that of zone A. In a word, Zone C is an appropriate secure zone for thermal processing.

(iv) The SEM micrograph corresponding to Zone D1 (deformation temperature is 800 °C and the strain rate is 10 s^{-1}), where m is about 0.2 and η is 2%, is shown in Fig. 3(d). Owing to the lower deformation temperature and higher strain rate, the efficiency is much smaller than those corresponding to the power dissipation zones of A and C. Both dynamic recrystallization and dynamic recovery will not occur. The prior austenite grains are elongated in the direction of deformation. The flow instability mechanisms, such as wedge cracking, adiabatic shear band, and prior particle boundary, are responsible for the flow instability. Meanwhile, at low temperatures and high strain rates, instability owing to

TABLE III. The measured grain sizes after different thermal deformations of the explored type 347H austenitic steel.

Strain rate (s^{-1})	0.01	0.1	1	10
The mean grain size (μm)	13.24	12.18	7.86	6.53

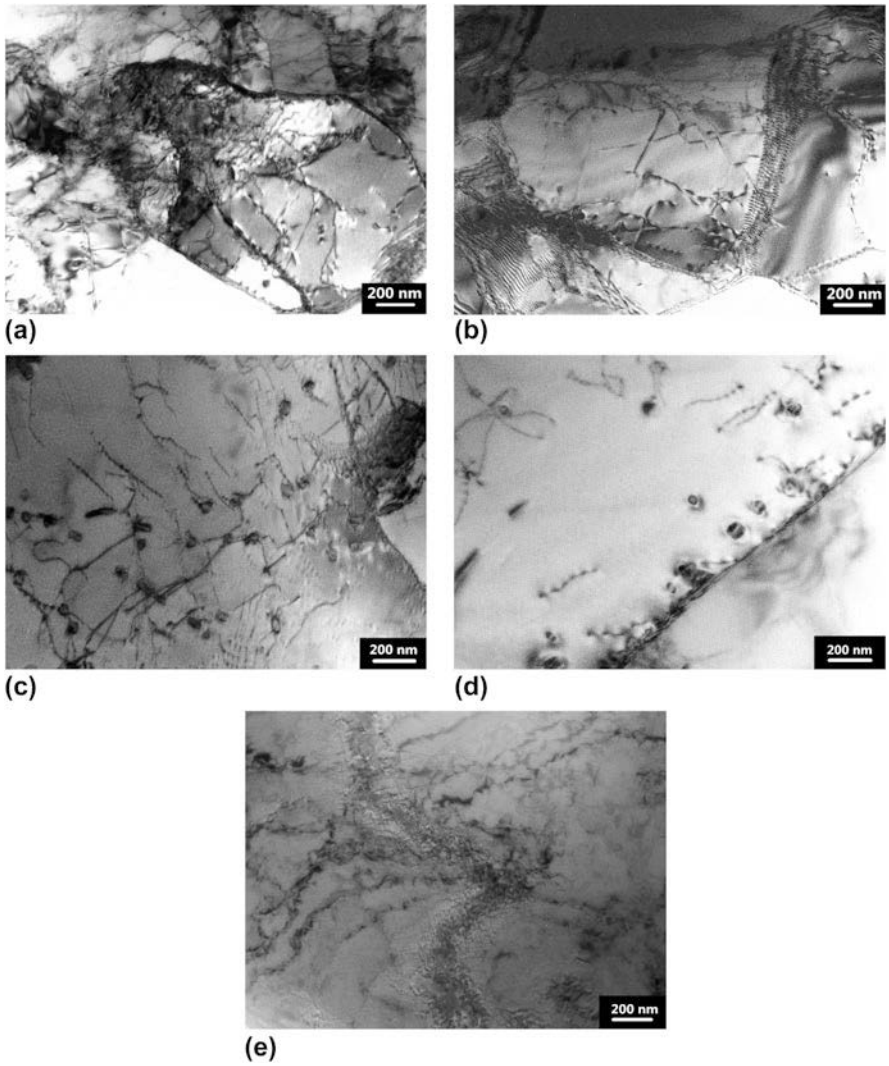

FIG. 5. The TEM micrographs of the type 347H austenitic steel after thermal deformation, (a) recrystallized grain, (b) dislocation walls and lines, (c) MX carbides precipitate at dislocation lines and dislocations, (d) MX carbides distributing around grain boundaries, and (e) flow localization.

adiabatic shear band formation is possible. So this zone is not suitable for thermal processing.

(v) The SEM micrograph corresponding to Zone D2 (deformation temperature is 800 °C and the strain rate is 0.01 s^{-1}), where *m* is about 0.02 and η is 2%, is shown in Fig. 3(e). The *m* and the efficiency are close to those of Zone B, which is related to the low strain rate and temperature. In this sample, local flow phenomenon can be observed, and austenite grain is squeezed in a direction perpendicular to the stress. Dynamic recrystallization and recovery will not occur. The local flow phenomenon is considered to be a precursor of material failure, and microcracks begin to nucleate and expand in the steels.[28,29] Thus, D2 is also an unstable zone for thermal deformation.

D. The influence of deformation temperature on the matrix of type 347H austenitic steel

Deformation temperature and strain rate are two predominant parameters during thermal deformation, both of which contribute to the microstructure evolution of the austenitic steel. Figure 4 shows the microstructures of the samples under different deformation conditions. As seen from Fig. 4(a), the microstructure after quenching is the homogeneous austenite with a small amount of twin crystals, and the austenite grain size is about 22 μm. After the solution treatment, the samples were deformed at 800 °C with a strain rate of 0.01 s^{-1}. Figure 4(b) demonstrates the elongated austenite grains, and few dynamic recrystallized grains can be observed in the matrix. When the deformation temperature was increased to 1000 °C, local recrystallization occurred at the prior grain boundaries. From Fig. 4(c), various degrees of recrystallization region can be found in the austenite matrix. When the deformation temperature is up to 1100 °C, the samples have undergone an adequate dynamic recrystallization. The grain size is very fine and the average grain size is about 14 μm [see Fig. 4(d)]. At the same strain rate, increase of deformation temperature promotes the dynamic recrystallization. Since the low deformation temperature is not beneficial to the migration of grain boundaries, the incubation period of dynamic recrystallization extends, and the nucleation and growth rates of the dynamic recrystallized grains decrease.[30] Actually, there occurs no dynamic recrystallization at low deformation temperatures. Increase of temperature can promote the occurrence of dynamic recrystallization.

E. The influence of strain rate on the matrix of type 347H austenitic steel

The SEM micrographs of the samples deformed at 1100 °C with various strain rates are shown in

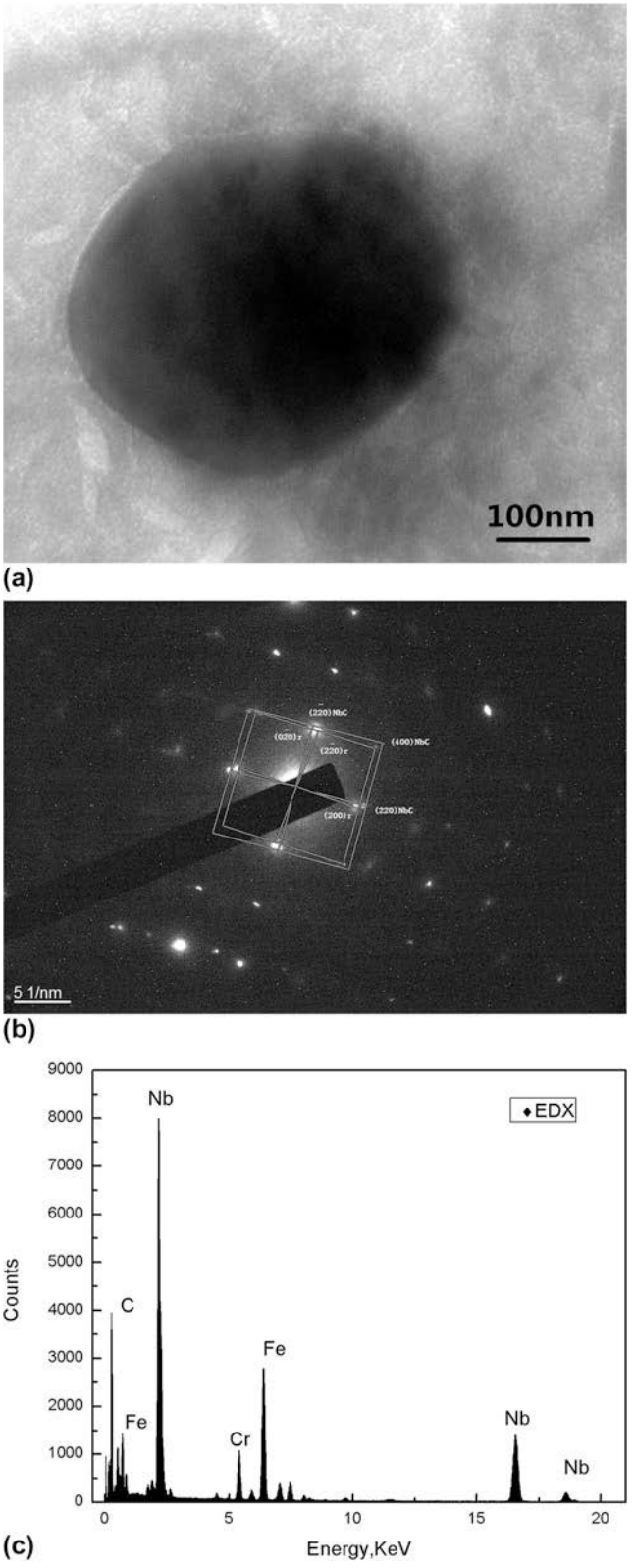

FIG. 6. The diffraction pattern and energy spectrum of NbC, (a) the TEM micrograph of NbC, (b) the diffraction pattern of NbC, and (c) the energy spectrum of NbC.

Figs. 4(d)–4(g). With respect of the strain rates at 0.01 to 10 s^{-1}, due to the high-strain rates and high-deformation temperature, the amount of recrystallization grains tends to decrease. With the strain rate decreasing, the recrystallized grains grow faster. At the strain rates of 0.01 and 0.1 s^{-1}, dynamic recrystallization occurs [see Figs. 4(d) and 4(e)], as the high temperature promotes the diffusion of atoms and low strain rates provide full time to grow up. Some grains are combined together in the matrix. Obviously, the grain size deformed at 0.01 s^{-1} is larger. When the strain rate is 1 s^{-1}[see Fig. 4(e)], the grain size is greatly refined. Specially, the dynamic recrystallization cannot undergo completely when the strain rate is 10 s^{-1}. As shown in Fig. 4(g), at high-strain rate, there is not enough time for full recrystallization, and the recrystallized grains have little time to grow up. Table III gathers the grain sizes of the samples deformed at 1100 °C under various strain rates. The faster the strain rate is the smaller the grain size will be.

F. Effects of thermal deformation on the precipitation behavior of MX carbides

To better understand the microstructural evolution of type 347H steel during thermal deformation, combining the hot processing maps, TEM images of samples deformed at 1100 °C and 1 s^{-1} are presented in Fig. 5. Dynamic recrystallized grains can be observed in Fig. 5(a). In the matrix, dislocations-tangling phenomenon is evident. There appear a great many of small dislocation lines and walls, as shown in Fig. 5(b). Therefore, thermal deformation can facilitate more favorable nucleation sites of MX carbides, contributing to the precipitation of more carbides.[31–33] After thermal deformation, the amount of carbides in the austenite matrix increases. Particles are aggregated at the dislocation lines, indicating that the MX

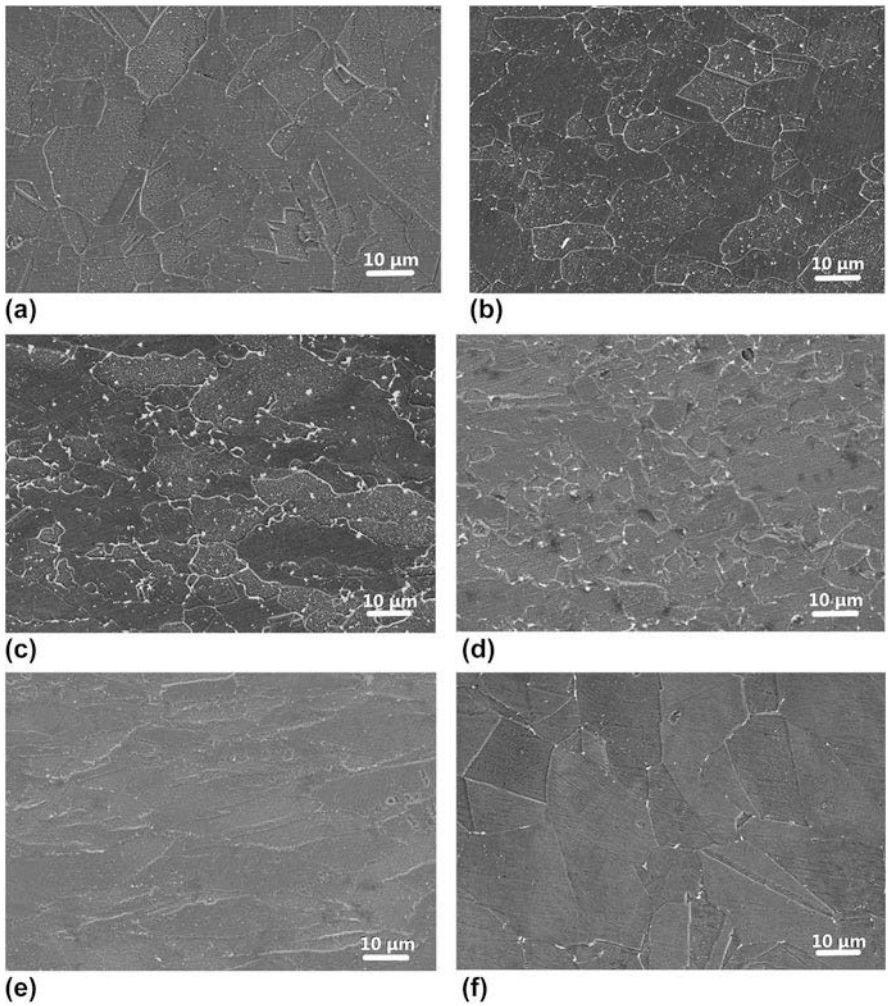

FIG. 7. The SEM micrographs of the type 347H austenitic steel samples, which deformed under different conditions aging at 700 °C for one hour, (a) aging at 700 °C for one hour, (b) aging at 700 °C for one hour after deforming at 1100 °C and 0.01 s^{-1}, (c) aging at 700 °C for one hour after deforming at 1100 °C and 1 s^{-1}, (d) aging at 700 °C for one hour after deforming at 1100 °C and 10 s^{-1}, (e) aging at 700 °C for one hour after deforming at 800 °C and 0.01 s^{-1}, and (f) aging at 700 °C for one hour after deforming at 800 °C and 10 s^{-1}.

carbides nucleate at dislocation lines and are tangled together with dislocations [see Fig. 5(c)]. Meanwhile, the MX carbides are also observed at the grain boundaries [see Fig. 5(d)], suggesting that the grain boundaries may not be the preferred nucleation location of MX carbides. MX carbides are uniformly distributed in the matrix and can be observed both at the grain boundaries and within grain interior. According to the diffraction pattern and energy spectrum results in Fig. 6, these square particles can be identified as NbC (MX type carbides). TEM micrograph of the sample deformed at 800 °C and 10 s^{-1}, corresponding to an unstable zone, is shown in Fig. 6(e). Recrystallization phenomenon is not observed, and there is not a large amount of dislocation. Only some processing flow lines and fine carbides can be found in the austenite matrix.

From the TEM micrographs, there is no doubt that thermal deformation can provide more nucleation sites in the austenite matrix and accelerate the precipitation of carbides. The SEM micrographs of samples after hot deformation demonstrate that the samples deformed in the secure regions precipitate more carbides than that in the unstable conditions. Figure 7 shows the SEM images of the undeformed and the deformed samples after aging at 700 °C for an hour. For the sample without deformation, there is small amount of carbides precipitate in the matrix [see Fig. 7(a)]. Figures 7(b)–7(d) represent the micrographs of the samples deformed under secure parameters and then aged under the same condition. Figure 7(e) represents the microstructures of the samples deformed under unstable parameters and then aged at 700 °C for an hour. According to the Figs. 7(b)–7(d), it can be obviously found that the amount of the carbides of the sample under the conditions corresponding to secure zone is much more than that under the unstable deformation conditions. Moreover, after isothermal aging, more carbide particles are precipitated in the deformed samples than that without thermal deformation. In comparison with the samples deformed under the conditions corresponding to secure zone, dynamic recrystallization and recovery will not occur under the conditions corresponding to unstable region, except for flow unstable lines and elongated grains. On one hand, the dynamic recrystallization promotes the formation of fine grains and results in the increase of the area of grain boundaries. The number of nucleation sites of MX carbide will also increase. On the other hand, the dislocation density corresponding to secure zone is obviously greater than that corresponding to unstable region, and the dislocation lines and walls will also be increased. These also provide more favorable sites for the carbide nucleation. After aging followed by thermal deformation, the grain size corresponding to unstable region is large, and precipitates are distributed uniformly. However, the amount of carbides is small. For samples deformed corresponding to safe zone, the amount of carbides increases significantly and no twins are observed. Austenite grains cannot be distinguished clearly, since the shape of grains is equiaxed rather than flat grain boundary. Meanwhile, the grain boundaries can be pinned by uniformly distributed fine carbides, and the steel will exhibit better plasticity and toughness.

IV. CONCLUSIONS

In this study, the thermal deformation behaviors of the type 347H austenitic stainless steel are investigated under the deformation temperatures from 800 to 1100 °C and the strain rates from 0.01 to 10 s^{-1}. The following conclusions can be drawn from the above results:

(1) The constitutive equation of type 347H austenitic heat-resistant steel is determined, and the deformation activation of the type 347H austenitic steel is 555.1 kJ.

(2) The secure zone of type 347H austenitic steel mainly consists of the deformation conditions incorporating deformation temperature of about 1000 °C and the strain rate of 1 s^{-1} or less. While the unstable zone mainly consists of the deformation conditions combining lower deformation temperatures and higher strain rates. Hot processing parameters should be preferred to a relatively large m and high-energy dissipation efficiency.

(3) If dynamic recrystallization undergoes completely at the deformation temperature of 1100 °C, the greater the strain rate is the smaller the grain size will be. Meanwhile, the increased deformation temperature promotes the initiation of dynamic recrystallization.

(4) Compared with the samples without thermal deformation, more NbCs will precipitate in the austenite matrix. Furthermore, the type 347H steel deforms in stable regions and precipitates more NbC than in the unstable regions.

ACKNOWLEDGMENTS

The authors are grateful to the China National Funds for Distinguished Young Scientists (Grant No. 51325401), the International Thermonuclear Experimental Reactor (ITER) Program Special Project (Grant No. 2014GB125006), the National High Technology Research and Development Program ("863"Program) of China (Granted No. 2015AA042504), the National Natural Science Foundation of China (Grant No. 51474156), and the Natural Science Foundation of Tianjin City (Grant No. 12JCYBJC11800) for grant and financial support.

REFERENCES

1. Z.H. Wang, W.T. Fu, B.Z. Wang, W.Z. Wang, W.H. Zhang, Z.Q. Lv, and P. Jiang: Study on hot deformation characteristics of 12%Cr ultra-super-critical rotor steel using processing maps and Zener–Hollomon parameter. *Mater. Charact.* **61**, 25 (2010).

2. J.D. Tian, Q.W. Cai, H.B. Wu, and Y. Ren: Effect of Nb on austenite recrystallization in high temperature deformation process. *J. Iron Steel Res. Int.* **17**, 39 (2010).
3. K.H. Lo, C.H. Shek, and J.K.L. Lai: Recent developments in stainless steels. *Mater. Sci. Eng., R* **65**, 39 (2009).
4. V. Moura, A.Y. Kina, S.S.M. Tavares, L.D. Lima, and F.B. Mainier: Influence of stabilization heat treatments on microstructure, hardness and intergranular corrosion resistance of the AISI 321 stainless steel. *J. Mater. Sci.* **43**, 536 (2008).
5. C.Y. Wang, X.J. Wang, and H. Chang: Processing maps for hot working of ZK60 magnesium alloy. *Mater. Sci. Eng., A* **43**, 77 (2007).
6. S.Q. Lu, X. Li, and K.L. Wang: Dynamic material model theory and its application for controlling microstructures and properties of hot worked materials. *Chin. J. Mech. Eng.* **43**, 77 (2007).
7. Vu The Ha and W.S. Jung: Creep behavior and microstructure evolution at 750 °C in a new precipitation-strengthened heat-resistant austenitic stainless steel. *Mater. Sci. Eng., A* **558**, 103 (2012).
8. D.B. Park, M.Y. Huh, W.S. Jung, J.Y. Suh, J.H. Shim, and S.C. Lee: Effect of vanadium addition on the creep resistance of 18Cr9Ni3CuNbN austenitic stainless heat resistant steel. *J. Alloys Compd.* **574**, 532 (2013).
9. Y.H. Liu, Y.Q. Ning, Z.K. Yao, H.Z. Guo, and Y. Nan: Effect of true strains on processing map for isothermal compression of Ni–20.0Cr–2.5Ti–1.5Nb–1.0Al Ni-base superalloy. *J. Alloys Compd.* **612**, 56 (2014).
10. R.K.C. Nkhoma, C.W. Siyasiya, and W.E. Stumpf: Hot workability of AISI 321 and AISI 304 austenitic stainless steels. *J. Alloys Compd.* **595**, 103 (2014).
11. A.I. Zaky Farahat, T. El-Bitar, and E. El-Shenawy: Austenitic stainless steel bearing Nb compositional and plastic deformation effects. *Mater. Sci. Eng., A* **492**, 161 (2008).
12. A. Momeni and K. Deghani: Characterization of hot deformation behavior of 410 martensitic stainless steel using constitutive equations and processing maps. *Mater. Sci. Eng., A* **527**, 5467 (2010).
13. A. Momeni and K. Deghani: Hot working behavior of 2205 austenite–ferrite duplex stainless steel characterized by constitutive equations and processing maps. *Mater. Sci. Eng., A* **528**, 1448 (2011).
14. A. Mirzaei, A. Zarei- Hanzaki, N. Haghdadi, and A. Marandi: Constitutive description of high temperature flow behavior of Sanicro-28 super-austenitic stainless steel. *Mater. Sci. Eng., A* **589**, 76 (2014).
15. S. Kim, Y.C. Yoo, and B-L. Jang: Modeling of recrystallization and austenite grain size for AISI 316 stainless steel and its application to hot bar rolling. *Mater. Sci. Eng., A* **311**, 108 (2001).
16. E.S. Silva, R.C. Sousa, A.M. Jorge, Jr., and O. Balancin: Hot deformation behavior of an Nb- and N-bearing austenitic stainless steel biomaterial. *Mater. Sci. Eng., A* **543**, 69 (2012).
17. Z. Yanushkevich, A. Belyakov, and R. Kaibyshev: Microstructural evolution of a 304-type austenitic stainless steel during rolling at temperatures of 773–1273 K. *Acta Mater.* **82**, 244 (2015).
18. Y.B. Yang, Z.P. Xie, Z.M. Zhang, X.B. Li, Q. Wang, and Y.H. Zhang: Processing maps for hot deformation of the extruded 7075 aluminum alloy bar: Anisotropy of hot workability. *Mater. Sci. Eng., A* **615**, 183 (2014).
19. J.Z. Wang, Z.D. Liu, S.C. Chang, and H.S. Bao: Hot deformation behaviors of S31042 austenitic heat resistant steel. *J. Iron Steel Res. Int.* **18**, 54 (2011).
20. O. Sivakesavam and Y.V.R.K. Prasad: Processing map for hot working of hot rolled Mg-11.5Li-1.5Al alloy. *Z. Metallkd.* **93**, 123 (2002).
21. J. Moon, T-H. Lee, J-H. Shin, and J-W. Lee: Hot working behavior of a nitrogen-alloyed Fe-18Mn-18Cr-N austenitic stainless steel. *Mater. Sci. Eng., A* **594**, 302 (2014).
22. A. Dehghan-Manshadi, M.R. Barnett, and P.D. Hodgson: Recrystallization in AISI 304 austenitic stainless steel during and after hot deformation. *Mater. Sci. Eng., A* **485**, 664 (2008).
23. H.Y. Sun, Y.D. Sun, R.Q. Zhang, M. Wang, R. Tang, and Z.J. Zhou: Hot deformation behavior and microstructural evolution of a modified 310 austenitic steel. *Mater. Des.* **67**, 165 (2015).
24. S.P. Tan, Z.H. Wang, S.C. Cheng, Z.D. Liu, J.C. Han, and W.T. Fu: Processing maps and hot workability of Super304H austenitic heat-resistant stainless steel. *Mater. Sci. Eng., A* **517**, 312 (2009).
25. G.W. Liu, Y. Han, Z.Q. Shi, J.P. Sun, D. Zou, and G.J. Qiao: Hot deformation and optimization of process parameters of an as-cast 6Mo super austenitic stainless steel: A study with processing map. *Mater. Des.* **53**, 662 (2014).
26. E.X. Pu, W.J. Zheng, J.Z. Xiang, Z.G. Song, and J. Li: Hot deformation characteristic and processing map of super austenitic stainless steel S32654. *Mater. Sci. Eng., A* **598**, 174 (2014).
27. Z.H. Wang, S.H. Sun, B. Wang, Z.P. Shi, and W.T. Fu: Effect of grain size on dynamic recrystallization and hot-ductility behaviors in high-nitrogen CrMn austenitic stainless steel. *Metall. Mater. Trans. A* **45A**, 3363 (2014).
28. D. Samantaray, S. Mandal, and A.K. Bhaduri: Optimization of hot working parameters for thermo-mechanical processing of modified 9Cr–1Mo (P91) steel employing dynamic materials model. *Mater. Sci. Eng., A* **528**, 5204 (2011).
29. H.Y. Sun, Y.D. Sun, R.Q. Zhang, M. Wang, R. Tang, and Z.J. Zhou: Study on hot workability and optimization of process parameters of a modified 310 austenitic stainless steel using processing maps. *Mater. Des.* **64**, 374 (2014).
30. S.M. Hong, M.Y. Kim, D.J. Min, K.H. Lee, J.H. Shim, D.I. Kim, J.Y. Suh, W.S. Jung, and I.S. Choi: Unraveling the origin of strain-induced precipitation of $M_{23}C_6$ in the plastically deformed 347 austenite stainless steel. *Mater. Charact.* **94**, 7 (2014).
31. A. Momeni, K. Dehghani, H. Keshmiri, and G.R. Ebrahimi: Hot deformation behavior and microstructural evolution of a super austenitic stainless steel. *Mater. Sci. Eng., A* **527**, 1605 (2010).
32. P. Behjati, A. Kermanpur, A. Najafizadeh, and H.S. Baghbadorani: Influence of nitrogen alloying on properties of Fe–18Cr–12Mn–XN austenitic stainless steels. *Mater. Sci. Eng., A* **618**, 16 (2014).
33. Y. Wang, X.G. Zhang, L.G. Meng, H. Zhu, M. Zhao, and N. Jiang: The microstructure and properties evolution of Al-Si/Al-Mn clad sheet during plastic deformation. *J. Mater. Res.* **28**, 1601 (2013).